

STABILIZING CLOUD FEEDBACK DRAMATICALLY EXPANDS THE HABITABLE ZONE OF TIDALLY LOCKED PLANETS

JUN YANG

The Department of the Geophysical Sciences, The University of Chicago, 5734 South Ellis Avenue, Chicago, IL 60637, USA

NICOLAS B. COWAN

Center for Interdisciplinary Exploration and Research in Astrophysics (CIERA) and Department of Physics and Astronomy, Northwestern University, 2131 Tech Drive, Evanston, IL 60208, USA

AND

DORIAN S. ABBOT

The Department of the Geophysical Sciences, The University of Chicago, 5734 South Ellis Avenue, Chicago, IL 60637, USA

Draft version July 19, 2013

ABSTRACT

The Habitable Zone (HZ) is the circumstellar region where a planet can sustain surface liquid water. Searching for terrestrial planets in the HZ of nearby stars is the stated goal of ongoing and planned extrasolar planet surveys. Previous estimates of the inner edge of the HZ were based on one dimensional radiative-convective models. The most serious limitation of these models is the inability to predict cloud behavior. Here we use global climate models with sophisticated cloud schemes to show that due to a stabilizing cloud feedback, tidally locked planets can be habitable at twice the stellar flux found by previous studies. This dramatically expands the HZ and roughly doubles the frequency of habitable planets orbiting red dwarf stars. At high stellar flux, strong convection produces thick water clouds near the substellar location that greatly increase the planetary albedo and reduce surface temperatures. Higher insolation produces stronger substellar convection and therefore higher albedo, making this phenomenon a stabilizing climate feedback. Substellar clouds also effectively block outgoing radiation from the surface, reducing or even completely reversing the thermal emission contrast between dayside and nightside. The presence of substellar water clouds and the resulting clement surface conditions will therefore be detectable with the James Webb Space Telescope.

1. INTRODUCTION

Water clouds influence the climate and habitability of a planet by either scattering incoming stellar radiation back to space (cooling) or by absorbing and reradiating thermal emission from the surface (warming). Near the cold outer edge of the HZ (Kasting et al. 1993), CO₂ ice clouds can scatter outgoing thermal radiation back to the surface, also causing warming (Forget & Pierrehumbert 1997; Wordsworth et al. 2011). Near the hot inner edge of the HZ, water vapor becomes a major component of the atmosphere and dominates its infrared opacity. Water clouds would therefore have a weak greenhouse effect in this regime (Kasting 1988), but may significantly increase planetary albedo (Selsis et al. 2007; Kaltenecker et al. 2011).

Previous investigations of the inner edge of the HZ have typically been based on 1D radiative-convective models that neglect cloud effects (Kasting et al. 1993; Kopparapu et al. 2013). Recently, one dimensional (1D) cloud models were developed to investigate the effects of clouds on exoplanet climate (Kitzmann et al. 2010; Zsom et al. 2012). These models incorporate a treatment of cloud microphysics, but cannot predict cloud coverage, location, or altitude, all of which are essential for determining cloud radiative effects. Such cloud features can only be predicted by making 3D dynamical calculations of atmospheric circulation. A few studies

with 3D general circulation models (GCMs) have simulated clouds of tidally locked planets at low stellar fluxes (Joshi 2003; Edson et al. 2011, 2012), but the impact of 3D cloud behavior on the inner edge of the HZ has not been considered. Here we study this issue using GCMs that explicitly calculate atmospheric dynamics, radiative transfer, the hydrological cycle, and clouds.

We focus on planets around M dwarf stars, which have small masses, low photospheric temperatures, and constitute $\approx 75\%$ of main sequence stars. Current data suggest there is ≈ 1 Earth-size planet in the HZ per M-star (Dressing & Charbonneau 2013; Morton & Swift 2013), and these planets are relatively easy to detect by radial velocity and transit surveys (Charbonneau & Deming 2007). Because tidal forces are strong at short distances, habitable planets in circular orbits around low-mass stars are expected to be tidally locked, with one hemisphere experiencing perpetual day and the other perpetual night.

2. GLOBAL CLIMATE MODELS

We perform simulations using 3D GCMs with sophisticated cloud schemes. The climate models we use include atmospheric GCMs: the Community Atmosphere Model version 3.1 (CAM3; Collins et al. 2004), version 4.0 (CAM4; Neale et al. 2010a), and version 5.0 (CAM5; Neale et al. 2010b) coupled with a mixed layer (immobile) ocean with a uniform depth of 50 meters, and a fully coupled atmosphere-ocean GCM: the Community Cli-

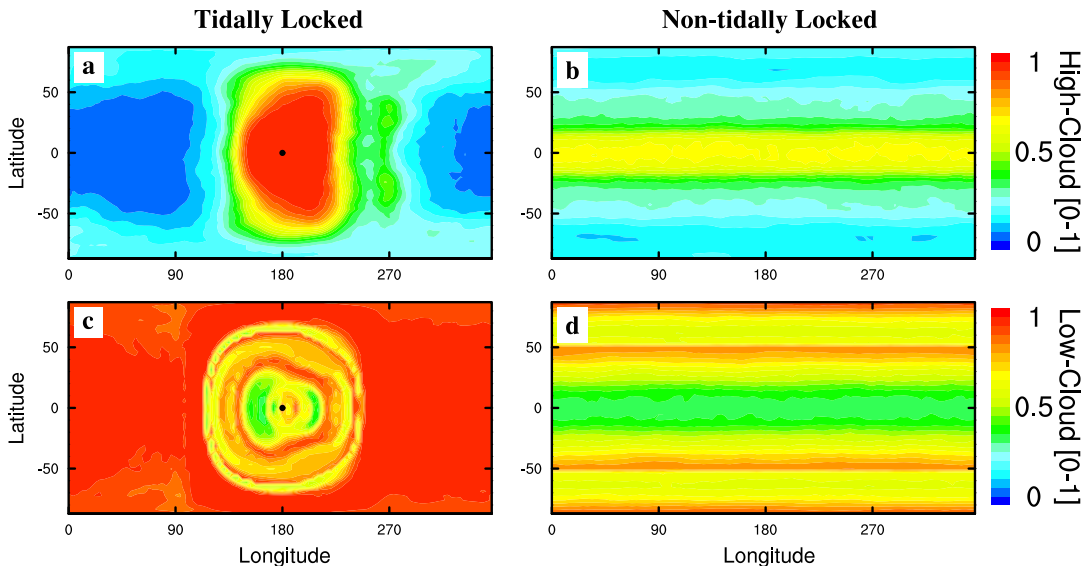


FIG. 1.— Cloud behavior for tidally (left) and non-tidally (right) locked planets. High-level cloud fraction (top) and low-level cloud fraction (bottom) are displayed in each case. The non-tidally locked case is in a 6:1 spin-orbit resonance. The stellar flux is 1400 W m^{-2} . The black dot in (a & c) is substellar point.

mate System Model version 3.0 (CCSM3; Collins et al. 2006) with a uniform ocean depth of 4000 m. All the GCMs simulate marine stratus, layered clouds, shallow and deep convective clouds in both liquid and ice phases. CAM4 has a new deep-convection scheme relative to CAM3, and CAM5 has a completely new cloud parameterization that is different from CAM3 and CAM4. CAM5 attempts to simulate full aerosol-cloud interactions.

CAM3 solves the equations for atmospheric motion on a rotating sphere and the equations for radiative transfer including the effects of water vapor, greenhouse gases and clouds. The radiative scheme is accurate for atmospheres with CO_2 concentration up to ≈ 0.1 bar (Abbot et al. 2012b) and water vapor column content less than 1200 kg m^{-2} (Pierrehumbert 2010); in all our simulations CO_2 and water vapor are below these limits. Cloud absorption and shortwave scattering are represented in terms of cloud water content, cloud fraction and droplet effective radius. Cloud infrared scattering is not included as it is negligible (Fu et al. 1997) due to high infrared absorption by water clouds (Pierrehumbert 2010). Cloud fraction is parameterized based on relative humidity, atmospheric stability and convective mass fluxes. Cloud water content is determined prognostically by a cloud microphysical scheme.

We have modified the models to be able to simulate the climates of extrasolar planets with different stellar spectra, orbits, and atmospheres. The stellar spectrum we use is for an M-star (or K-star) with an effective temperature of 3400 (or 4500) K, assuming a blackbody spectral distribution. The stellar flux is set to a sequence of values from 1000 to 2600 W m^{-2} , which corresponds to moving the planet closer to the central star. The geothermal heat flux is set to zero. By default, the radius, gravity and orbital period of the planet are set to $2 R_{\oplus}$ (R_{\oplus} is Earth radius), $1.4 g_{\oplus}$ (g_{\oplus} is Earth gravity) and 60 Earth days (E-days), respectively. Both the obliquity and eccentricity are set to zero. For tidally locked simulations, the

rotation period is equal to the orbital period (1:1). For non-tidally locked simulations, the spin-orbit resonance is set to 2:1 (or 6:1), meaning that the rotation frequency is 2 (or 6) times faster than the orbital frequency.

The default atmosphere is 1.0 bar of N_2 and H_2O . Assuming the silicate weathering hypothesis (Walker et al. 1981) is correct, the CO_2 level should be low near the inner edge of the HZ, although this depends on the presence and location of continents (Edson et al. 2012; Abbot et al. 2012a). We therefore set CO_2 to zero, as well as CH_4 , N_2O , and O_3 . Sensitivity tests with different CO_2 levels show that this has little effect on our results (Section 5). The experimental design for CAM4 and CAM5 is the same as CAM3 except that aerosols are set to zero in CAM3 and CAM4 but to 20th century Earth conditions in CAM5 because its cloud scheme requires aerosols.

We consider three idealized continental configurations in our ocean-atmosphere CCSM3 simulations: (i) aquaplanet: a globally ocean covered planet; (ii) one ridge: a thin barrier that completely obstructs ocean flow running from pole to pole on the eastern terminator; (iii) two ridges: two thin barriers on the western and eastern terminators, respectively. The planetary parameters for the CCSM3 simulations are a 37 E-days orbit period, a radius of $1.5 R_{\oplus}$, and gravity of $1.38 g_{\oplus}$ around an M-star.

3. THE STABILIZING CLOUD FEEDBACK

For tidally locked planets, most of the dayside is covered by clouds (Fig. 1) with a high cloud water content (several times Earth’s), arising from near-surface convergence and resulting convection at the substellar point. This circulation produces high-level and low-level clouds covering $\approx 60\%$ and 80% of the dayside, respectively. Since thick clouds occur right where the insolation is highest, they significantly increase the planetary albedo. Furthermore, the planetary albedo increases with the stellar flux (S_0) for planets around both M- and K-stars (Fig. 2), leading to a stabilizing cloud feedback

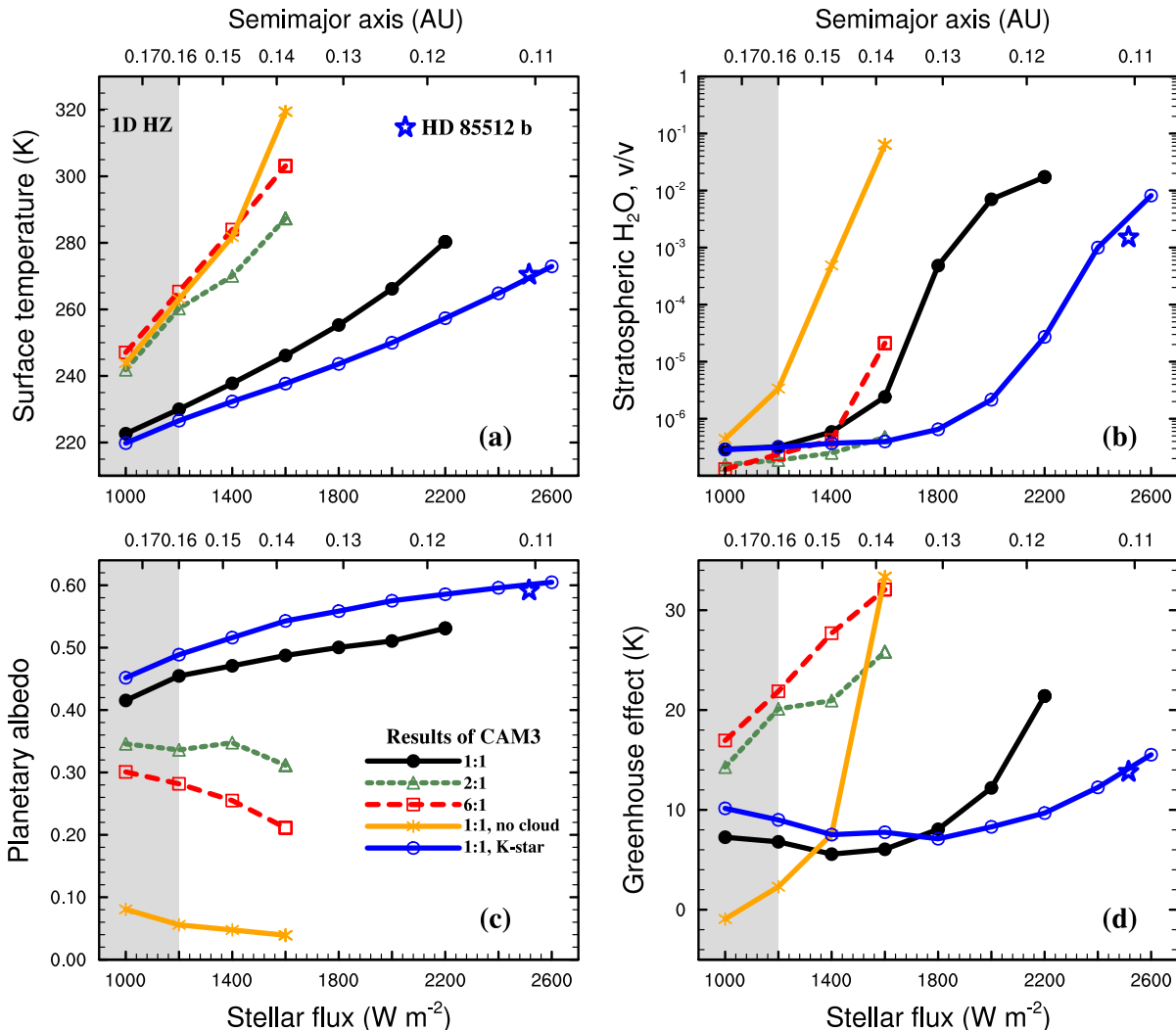


FIG. 2.— Climates of tidally locked and non-tidally locked terrestrial planets. (a) global-mean surface temperature (K), (b) stratospheric H_2O volume mixing ratio at the substellar point, (c) planetary albedo and (d) global-mean greenhouse effect (K). The upper horizontal axis is the corresponding semimajor axis between an M-star (with a $2.3\% L_\odot$) and the planet. 1:1 denotes a tidally locked state, and 2:1 and 6:1 denote 2 or 6 rotations per orbit, respectively. For “no cloud” cases, all clouds are set to zero. The stellar spectrum is for an M-star or an K-star. Results for HD 85512 b ($S_0 = 2515 \text{ W m}^{-2}$, $1.5 R_\oplus$, $1.6 g_\oplus$ and a 58 Earth-day orbit) are represented by a pentagram. The gray area denotes the HZ around an M-star with an inner edge of $S_0 \approx 1200 \text{ W m}^{-2}$ and an outer edge of $S_0 \approx 270 \text{ W m}^{-2}$ (not shown), obtained in a 1D model without clouds (Kopparapu et al. 2013).

on climate. This is due to increased convection at the substellar point as surface temperatures there increase. For an insolation of 2200 W m^{-2} and an M-star spectrum, the planetary albedo reaches 0.53, and the maximum surface temperature on the planet is only 305 K. The greenhouse effect from clouds is similar to that on Earth, with a global-mean value of $20\text{--}30 \text{ W m}^{-2}$. For a hotter K-star, the stellar spectrum is such that the planetary albedo is higher at all stellar fluxes and reaches 0.60 for $S_0 = 2600 \text{ W m}^{-2}$. Assuming HD 85512 b (Pepe et al. 2011) is tidally locked and Earth-like, our calculations suggest it has an albedo of 0.59 and a mean surface temperature of 271 K. The recently discovered super-Earth GJ 163 c (Bonfils et al. 2013), provided it is tidally locked, should also have a high albedo and therefore be habitable.

The cloud behavior for non-tidally locked planets contrasts markedly with that of tidally locked planets. Non-tidally locked planets have an albedo similar to Earth’s

(≈ 0.3). This is because only part of the tropics and the mid-latitudes are covered by clouds (Fig. 1) and the cloud water content is relatively small. In contrast to the tidally locked case, the planetary albedo decreases as S_0 is increased (Fig. 2c), representing a destabilizing feedback. This is primarily due to decreases in cloud coverage associated with reduced latitudinal temperature gradient and resulting weakened Hadley cells.

In order to clearly demonstrate the influence of clouds, we switch off the cloud module in the model and repeat the tidally locked simulations. At an insolation of 1600 W m^{-2} , the planetary albedo drops from 0.53 to 0.04, and the global-mean surface temperature rises from 246 to 319 K (Fig. 2a). Clouds therefore account for 73 K of cooling, which is critical for extending the HZ to higher stellar flux.

Tidally locked planets not only have a higher cloud albedo, but also a smaller greenhouse effect ($G = T_{em}^{stf} -$

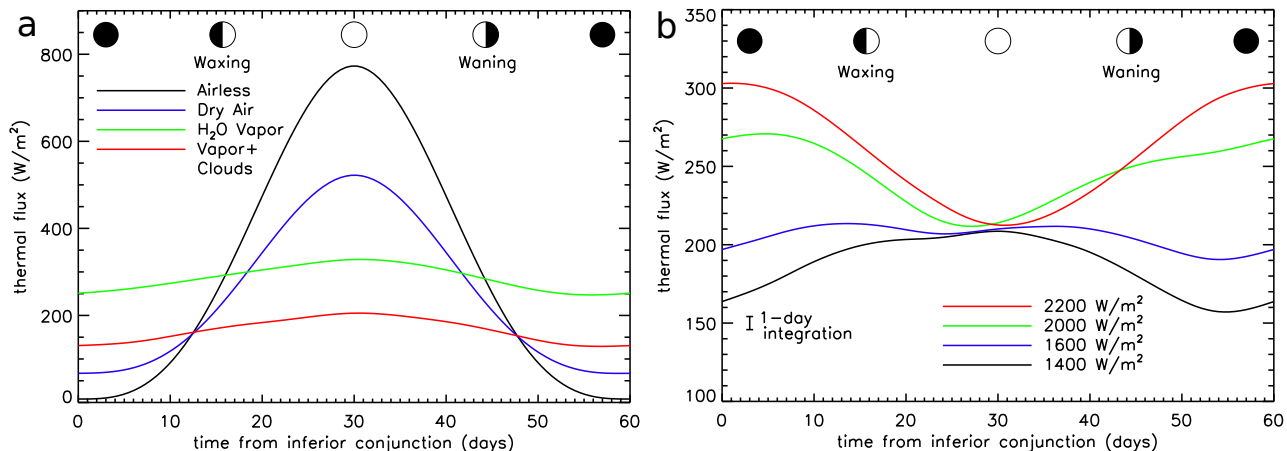


FIG. 3.— Thermal phase curves of tidally locked planets. (a) phase curves for different atmospheres with stellar flux fixed at 1200 W m^{-2} : airless, dry-air, water vapor, and water vapor plus clouds, (b) phase curves for a full atmosphere including water vapor and clouds for different stellar fluxes: 1400 , 1600 , 2000 and 2200 W m^{-2} . The error bar in (b) is the expected precision of the James Webb Space Telescope for observations of a nearby super-Earth. The surface albedo for the airless and dry-air cases is 0.2 . The orbital period is 60 Earth-days.

$$T_{ef}, \text{ where } T_{em}^{srf} = \left(\frac{F_{\uparrow}^{srf}}{\sigma} \right)^{\frac{1}{4}} \text{ and } T_{ef} = \left(\frac{F_{\uparrow}^{top}}{\sigma} \right)^{\frac{1}{4}},$$

where F_{\uparrow}^{srf} and F_{\uparrow}^{top} are the global mean upward infrared radiative fluxes at the surface and top of atmosphere, respectively). For reference, $G \approx 33 \text{ K}$ on modern Earth. The greenhouse effect for tidally locked planets is much smaller than those for non-tidally locked planets (Fig. 2d). This results from a low-level temperature inversion on the nightside of tidally-locked planets (see also Joshi et al. 1997; Leconte et al. 2013). The inversion is due to efficient radiative cooling by the surface on the nightside and strong atmospheric energy transport from the dayside to the nightside (Merlis & Schneider 2010). The outgoing infrared radiation to space is therefore similar to the near-surface upward infrared radiation, resulting in a small G .

Our results demonstrate that at high stellar flux, Earth-like tidally locked planets have a high planetary albedo, a low greenhouse effect, and therefore low enough surface temperatures to be habitable. The sub-stellar and global-mean surface temperatures in our simulations remain well below the 340 K moist greenhouse limit of Kopparapu et al. (2013), but the dayside stratospheric water-vapor mixing ratio in our hottest simulations (Fig. 2b) is comparable to the $\approx 3.0 \times 10^{-3}$ moist greenhouse limit suggested by Kasting et al. (1993). Future modeling including H_2O photolysis and hydrogen escape would be needed to determine the moist greenhouse threshold for tidally locked planets.

4. THERMAL PHASE CURVES

The key to observationally confirming the presence of substellar clouds is that they also affect the planet’s outgoing longwave radiation (OLR). Following Cowan et al. (2012b), we use the OLR maps from the GCMs to compute time-resolved, disk-integrated broadband thermal phase curves measured by a distant observer (Fig. 3). Interannual variability in OLR is less 1% for our simulations; we therefore use the long-term mean maps. The sub-observer latitude is set to zero. Although this corresponds to an edge-on orbit for a zero-obliquity planet, the transits and eclipses have been omitted for clarity.

An airless planet exhibits large-amplitude thermal phase variations with a peak at superior conjunction (Fig. 3a; see also Maurin et al. 2012). For the dry-air case, the peak thermal emission occurs slightly before superior conjunction because of equatorial superrotation (see also Selsis et al. 2011). This is qualitatively similar to the eastward displacement of 5° – 60° typical for hot Jupiters (Knutson et al. 2007; Crossfield et al. 2010; Cowan et al. 2012a; Maxted et al. 2013). Equatorial superrotation is a generic feature of tidally locked planets arising from strong day–night forcing (Showman & Polvani 2011).

Water vapor and clouds, however, dramatically modify the phase curves. Water vapor is advected east of the substellar point (Fig. 4), where it absorbs outgoing thermal radiation, which leads to a lightcurve maximum *after* superior conjunction (Fig. 3b). Substellar clouds also absorb thermal emission, producing a local minimum in OLR (Fig. 4f) that weakens or completely reverses the day–night thermal flux contrast (Fig. 3b). Note that as the stellar flux is varied, the thermal flux near superior conjunction stays roughly constant and equal to the high-level cloud emission flux, which corresponds to the temperature at the tropopause. If convective clouds occur on hot Jupiters, the interpretation of their thermal phase variations (e.g., Knutson et al. 2007) will have to be revisited.

To determine whether these phase curve features would be detectable by the James Webb Space Telescope (JWST), we estimate the expected signal-to-noise ratio. The contrast ratio over some band $[\lambda_1, \lambda_2]$ is given by

$$\frac{F_p}{F_*} = \left(\frac{R_p}{R_*} \right)^2 \frac{\int_{\lambda_1}^{\lambda_2} B(T_{ef}, \lambda) d\lambda}{\int_{\lambda_1}^{\lambda_2} B(T_*, \lambda) d\lambda}, \quad (1)$$

assuming that both the star and the planet emit as blackbodies. Adopting values of $R_p = 2R_{\oplus}$, $R_* = 0.2R_{\odot}$, $T_{ef} = 240 \text{ K}$, and $T_* = 3000 \text{ K}$, the band-integrated (10 – $28 \mu\text{m}$) contrast for the Mid-Infrared Instrument on JWST is 4.9×10^{-5} .

To estimate the photometric precision one can expect for JWST, we begin with the 4×10^{-5} precision obtained

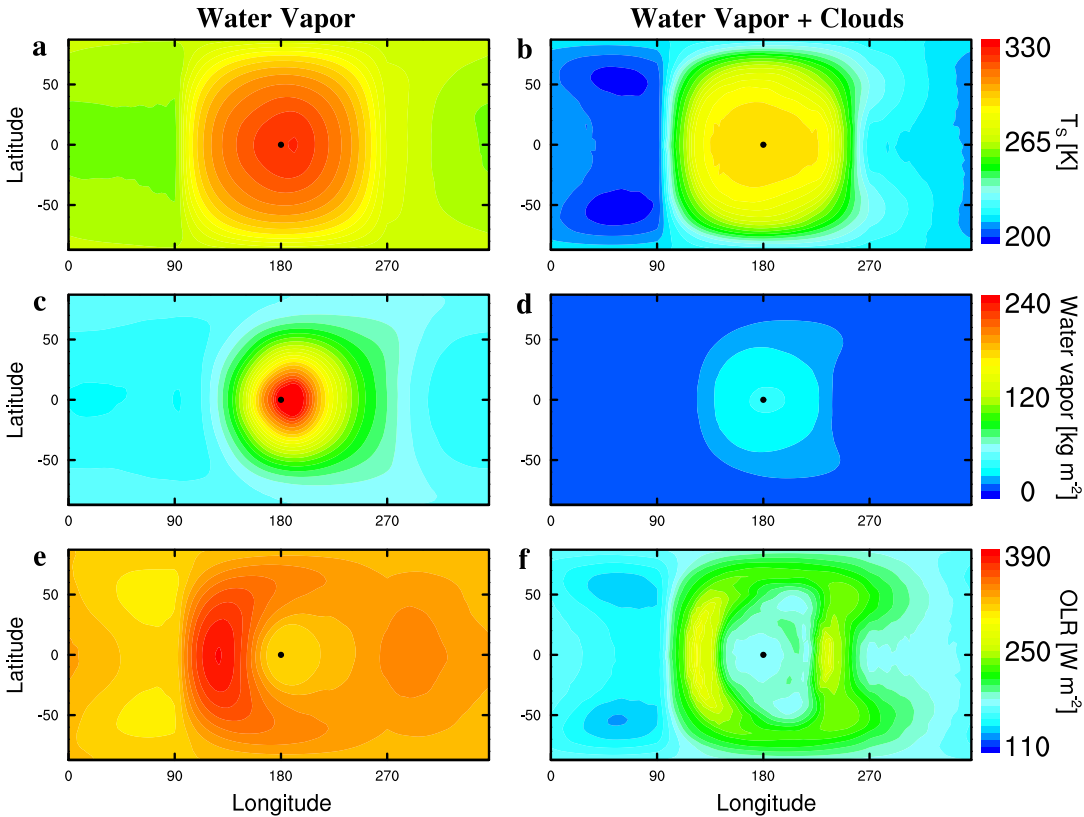


FIG. 4.— Water vapor and cloud behavior on a tidally locked terrestrial planet. Left panels: clouds are set to zero; right panels: clouds are interactively calculated. (a) and (b) surface temperature (T_S , K), (c) and (d) vertically integrated water vapor amount (kg m^{-2}), (e) and (f) outgoing longwave radiation at the top of the atmosphere (OLR, W m^{-2}). The stellar flux is 1400 W m^{-2} for all plots. The black dot is substellar point.

at $3.6 \mu\text{m}$ for HD 189733 with the Spitzer Space Telescope (Knutson et al. 2012). We then scale this by stellar flux and distance, integration time, and telescope size, assuming Poisson noise, $\sigma/F_* \propto 1/\sqrt{N}$. The number of photons is

$$N = \pi D^2 \tau \left(\frac{R_*}{d} \right)^2 \int_{\lambda_1}^{\lambda_2} \frac{B(T_*, \lambda)}{E(\lambda)} d\lambda \quad (2)$$

where $E(\lambda) = hc/\lambda$ is the energy per photon. We adopt the same values as above, in addition to $D = 6.5 \text{ m}$, $\tau = 1 \text{ day}$, and $d = 5$ or 20 pc (conservative distances to the nearest non-transiting and transiting M-Dwarf HZ terrestrial planets, respectively; Dressing & Charbonneau 2013). The expected photometric precision is 2.5×10^{-7} (non-transiting) and 1.0×10^{-6} (transiting). Note that the unknown radius and orbital inclination of non-transiting planets (Cowan et al. 2007; Crossfield et al. 2010) is not an obstacle for the current application because it is the lightcurve morphology, rather than amplitude, that betrays the presence of substellar clouds.

Dividing the contrast ratio by the precision estimates, we find that a 1-day integration with JWST could produce a 49σ detection of broadband planetary emission for a nearby transiting M-dwarf HZ planet (error bar in Fig. 3b).

5. SENSITIVITY TESTS

We have performed sensitivity experiments over a wide range of parameters, including cloud particle sizes, cloud

fraction parameters, surface pressure, CO_2 concentration, planetary radius, rotation rate, surface gravity, oceanic mixed layer depth, convective scheme, model resolution, land-sea distribution and ocean heat transport. Results are shown in Table 1. Both the planetary albedo and the spatial pattern of OLR are insensitive to changes in almost all of these parameters. In particular, most of our tests exhibit a high albedo and significant OLR minimum near the substellar point, especially at high stellar flux. Furthermore, simulations in a different GCM, GENESIS (Edson et al. 2011, 2012), also show a high albedo for tidally locked planets. This robustness is due to the simplicity of the mechanism: any GCM that produces strong convection at the substellar point should produce a high cloud albedo.

The stabilizing cloud albedo feedback is somewhat sensitive to three parameters. First, cloud albedo decreases if liquid cloud droplets are very large. In CAM3 and CAM4 the cloud droplet size is a specified parameter based on observations of modern Earth. If we double its value, the planetary albedo is reduced by ≈ 0.1 . It is unlikely that the droplet size would be this high, but it might be possible on a planet with extremely low levels of cloud condensation nuclei.

Second, if the orbital period is very short or the planetary radius is very large, then the Rossby deformation radius is smaller than the planetary radius and the atmospheric circulation is in the rapidly-rotating regime (Edson et al. 2011; Showman et al. 2013; Leconte et al. 2013), which results in concentrated convection and fewer dayside clouds. Quantitatively, we find that this regime

transition occurs at a 10-day orbit for a $2R_{\oplus}$ super-Earth, or a 5-day orbit for an Earth-sized planet. We therefore expect that the substellar cloud feedback we describe will be weaker for planets orbiting late-M dwarfs.

Third, the planetary albedo can be reduced if a large ocean heat transport (OHT) from the dayside to the nightside is added to CAM3. As the OHT is increased, the day–night surface temperature contrast decreases, weakening atmospheric circulation and producing less clouds. If the OHT is similar to that out of the tropics on modern Earth ($\approx 10 \text{ W m}^{-2}$; Trenberth & Caron 2001), the change in planetary albedo is negligible. To achieve a reduction in planetary albedo of ≈ 0.1 requires specifying an OHT ten times that on modern Earth. This implies that OHT would only disrupt the mechanism we describe on planets with thick oceans and few continents to disrupt ocean flows. We confirm this idea using our ocean-atmosphere simulations with CCSM3. For a thick ocean without continents, ocean circulation effectively transports heat from the dayside to the nightside and the planetary albedo is significantly reduced. The addition of obstructing continent(s), however, prevents OHT from disrupting the cloud feedback so that the planetary albedo is just as high as in CAM3 coupled with an immobile ocean.

As addressed in Section 4, substellar clouds could be inferred from thermal phase curves because of the suppressed dayside OLR. A potential false positive for this effect would be a planet with a dry atmosphere and a high surface albedo region near the substellar point. Such a configuration would reduce the surface temperature and, consequently, the OLR near the substellar point. We find

that in order to obtain similar dayside OLR patterns as those produced by substellar clouds, the substellar surface albedo must be ≈ 0.8 , which is implausible for planets around M-stars (Joshi & Haberle 2012; Shields et al. 2013). More importantly, such a planet would have much lower nightside OLR than the moist and cloudy planets considered here. It therefore seems that only clouds can create a significant OLR minimum at the substellar point in tandem with high nightside emission.

6. CONCLUSIONS

We have performed the first 3D global calculations of the effect of water clouds on the inner edge of the HZ and predict that tidally locked Earth-like planets have clement surface conditions at twice the stellar flux calculated by 1D models. This brings already detected planets, such as HD 85512 b and GJ 163 c, into the HZ, and dramatically increases estimates of the frequency of habitable planets. Adopting the planetary demographics from Figure 19 of Dressing & Charbonneau (2013), our revised inner edge of the HZ increases the frequency of habitable Earth-size planets by at least 50–100%. Crucially, we have also shown how this stabilizing cloud feedback can be tested in the near future with thermal phase curves from JWST.

We are grateful to D. Koll, Y. Wang, F. Ding, Y. Liu, C. Bitz, and R. Pierrehumbert for technical assistance and/or discussions. D.S.A. acknowledges support from an Alfred P. Sloan Research Fellowship.

REFERENCES

- Abbot, D. S., Cowan, N. B., & Ciesla, F. J. 2012a, *ApJ*, 756, 178
 Abbot, D. S., Voigt, A., Branson M., et al. 2012b, *Geophys. Res. Lett.*, 39, L20711.
 Bonfils, X., Lo Curto, G., Correia, A. C. M., et al. 2013, arXiv:1306.0904
 Charbonneau, D., & Deming, D. 2007, arXiv:0706.1047
 Collins, W. D., Basch, P. J., Boville, B. A., et al. 2004, Description of the NCAR Community Atmosphere Model (CAM) 3.0, NCAR-TN-464+STR, NCAR
 Collins, W. D., Bitz, C. M., Blackmon, M. L., et al. 2006, *J. Clim.*, 19, 2122
 Cowan, N. B., Agol, E., & Charbonneau, D. 2007, *MNRAS*, 379, 641
 Cowan, N. B., Machalek, P., Croll B., et al. 2012a, *ApJ*, 747, 82
 Cowan, N. B., Voigt, A., & Abbot, D. S. 2012b, *ApJ*, 757, 80
 Crossfield, I. M., Hansen, B. S., & Harrington, J., et al. 2010, *ApJ*, 723, 1436
 Dressing, C., & Charbonneau, D. 2013, *ApJ*, 767, 1
 Edson, A., Lee, S., Pollard, D., Bannon, P. R., & Kasting, J. F. 2011, *Icarus*, 212, 1
 Edson, A., Lee, S., Pollard, D., Bannon, P. R., & Kasting, J. F. 2012, *Astrobiology*, 12, 562
 Forget, F., & Pierrehumbert, R. T. 1997, *Science*, 278, 1273
 Fu, Q., Liou, K. N., Cribb, M. C., Charlock, T. P., & Grossman, A. 1997, *J. Atmos. Sci.*, 54, 2799
 Joshi, M. M. 2003, *Astrobiology*, 3, 415
 Joshi, M. M., Haberle, R. M., & Reynolds, R. T. 1997, *Icarus*, 129, 450
 Joshi, M. M., & Haberle, R. M. 2012, *Astrobiology*, 12, 3
 Kaltenecker, L., Udry, S., & Pepe, F. 2011, arXiv:1108.3561
 Kasting, J. F. 1988, *Icarus*, 74, 472
 Kasting, J. F., Whitmire, D. P., & Reynolds, R. T. 1993, *Icarus*, 101, 108
 Kitzmann, D., Patzer, A. B. C., vonParis, P., et al. 2010, *A&A*, 511, A66
 Kopparapu, R. K., Ramirez, R., Kasting, J. F., et al. 2013, *ApJ*, 767, 131
 Knutson, H. A., Charbonneau, D., Allen, L. E., et al. 2007, *Nature*, 447, 183
 Knutson, H. A., Lewis, N., Fortney, J. J., et al. 2012, *ApJ*, 754, 22
 Leconte, J., Forget, F., Charnay, B., et al. 2013, arXiv:1303.7079
 Maurin, A. S., Selsis, F., & Belu, A. 2012, *A&A*, 538, A95
 Maxted, P. F. L., Anderson, D. R., Doyle, A. P., et al. 2013, *MNRAS*, 428, 2645
 Merlis, T. M., & Schneider, T. 2010, *JAMES*, 2, 13
 Morton, T. D., & Swift, J. J. 2013, arXiv:1303.3013
 Neale, R. B., Richter, J. H., Conley, A. J., et al. 2010a, Description of the NCAR Community Atmosphere Model (CAM) 4.0, NCAR-TN-485+STR, NCAR
 Neale, R. B., Chen, C. C., Gettleman, A., et al. 2010b, Description of the NCAR Community Atmosphere Model (CAM) 5.0, NCAR-TN-486+STR, NCAR
 Pepe, F., Lovis C., Segransan, D., et al. 2011, *A&A*, 634, A58
 Pierrehumbert, R. T. 2010, *Principles of Planetary Climate* (Cambridge University Press)
 Selsis, F., Kasting, J. F., Levard, B., et al. 2007, *A&A*, 476, 1373
 Selsis, F., Wordsworth, R. D., & Forget, F. 2011, *A&A*, 532, A1
 Shields, A. L., Meadows, V. S., Bitz, C. M., et al. 2013, *Astrobiology*, submitted
 Showman, A. P., & Polvani, L. M. 2011, *ApJ*, 738, 71
 Showman, A. P., Wordsworth, R. D., Merlis, T. M., & Kaspi, Y. 2013, arXiv:0911.3170
 Trenberth, K. E., & Caron, J. M. 2001, *J. Clim.*, 14, 3433
 Walker, J. C. G., Hays, P. B., & Kasting, J. F. 1981, *J. Geophys. Res.*, 86, 9776
 Wordsworth, R. D., Forget, F., Selsis, F., et al. 2011, *ApJ*, 73, L48
 Zsom, A., Kaltenecker, L., & Goldblatt C. 2012, *Icarus*, 221, 603

TABLE 1
CLIMATE CHARACTERISTICS OF TERRESTRIAL PLANETS AROUND AN M-STAR

| Group | Model | Experimental Design | T_S^a (K) | Albedo ^b (0–1) | G^c (K) |
|----------------|-------|---|----------------|------------------------------|--------------|
| 1 ^d | CAM3 | an immobile ocean, $S_0 = 1600 \text{ W m}^{-2}$ | 246.7 | 0.48 | 4.9 |
| 1 | CAM4 | an immobile ocean, $S_0 = 1600 \text{ W m}^{-2}$ | 246.6 | 0.49 | 6.9 |
| 1 | CAM5 | an immobile ocean, $S_0 = 1600 \text{ W m}^{-2}$ | 240.0 | 0.49 | 3.1 |
| 2 ^e | CCSM3 | aqua-planet, dynamical ocean, $S_0 = 1600 \text{ W m}^{-2}$ | 296.2 | 0.26 | 27.6 |
| 2 | CCSM3 | 1 ridge, dynamical ocean, $S_0 = 1600 \text{ W m}^{-2}$ | 264.2 | 0.48 | 20.6 |
| 2 | CCSM3 | 2 ridges, dynamical ocean, $S_0 = 1600 \text{ W m}^{-2}$ | 263.0 | 0.49 | 20.6 |
| 3 ^f | CAM3 | spin:orbit = 1:1, $S_0 = 1000 \text{ W m}^{-2}$ | 222.6 | 0.42 | 7.3 |
| 3 | CAM3 | spin:orbit = 1:1, $S_0 = 1200 \text{ W m}^{-2}$ | 230.0 | 0.45 | 6.3 |
| 3 | CAM3 | spin:orbit = 1:1, $S_0 = 1400 \text{ W m}^{-2}$ | 237.8 | 0.47 | 5.6 |
| 3 | CAM3 | spin:orbit = 1:1, $S_0 = 1600 \text{ W m}^{-2}$ | 246.1 | 0.49 | 6.1 |
| 3 | CAM3 | spin:orbit = 1:1, $S_0 = 1800 \text{ W m}^{-2}$ | 255.3 | 0.50 | 8.1 |
| 3 | CAM3 | spin:orbit = 1:1, $S_0 = 2000 \text{ W m}^{-2}$ | 266.2 | 0.51 | 12.2 |
| 3 | CAM3 | spin:orbit = 1:1, $S_0 = 2200 \text{ W m}^{-2}$ | 280.3 | 0.53 | 21.4 |
| 4 ^g | CAM3 | spin:orbit = 2:1, $S_0 = 1000 \text{ W m}^{-2}$ | 241.8 | 0.35 | 14.3 |
| 4 | CAM3 | spin:orbit = 2:1, $S_0 = 1200 \text{ W m}^{-2}$ | 260.3 | 0.34 | 20.1 |
| 4 | CAM3 | spin:orbit = 2:1, $S_0 = 1400 \text{ W m}^{-2}$ | 270.0 | 0.35 | 20.9 |
| 4 | CAM3 | spin:orbit = 2:1, $S_0 = 1600 \text{ W m}^{-2}$ | 287.4 | 0.31 | 25.8 |
| 5 ^h | CAM3 | spin:orbit = 6:1, $S_0 = 1000 \text{ W m}^{-2}$ | 247.1 | 0.30 | 16.9 |
| 5 | CAM3 | spin:orbit = 6:1, $S_0 = 1200 \text{ W m}^{-2}$ | 265.4 | 0.28 | 21.9 |
| 5 | CAM3 | spin:orbit = 6:1, $S_0 = 1400 \text{ W m}^{-2}$ | 284.0 | 0.25 | 27.7 |
| 5 | CAM3 | spin:orbit = 6:1, $S_0 = 1600 \text{ W m}^{-2}$ | 303.1 | 0.21 | 32.1 |
| 6 ⁱ | CAM3 | control ($S_0 = 1200 \text{ W m}^{-2}$) | 230.0 | 0.45 | 6.3 |
| 6 | CAM3 | ice cloud particle size $\times 0.5$ | 229.1 | 0.47 | 7.0 |
| 6 | CAM3 | ice cloud particle size $\times 2.0$ | 230.3 | 0.44 | 5.1 |
| 6 | CAM3 | liquid cloud particle size = $3.5 \mu\text{m}$ | 219.6 | 0.54 | 7.0 |
| 6 | CAM3 | liquid cloud particle size = $7 \mu\text{m}$ | 223.7 | 0.51 | 6.7 |
| 6 | CAM3 | liquid cloud particle size = $28 \mu\text{m}$ | 241.8 | 0.34 | 5.1 |
| 6 | CAM3 | cloud parameter $RH_{min}^{high} - 10\%$ | 229.8 | 0.46 | 6.3 |
| 6 | CAM3 | cloud parameter $RH_{min}^{high} + 10\%$ | 230.2 | 0.45 | 6.0 |
| 6 | CAM3 | cloud parameter $RH_{min}^{low} - 10\%$ | 228.6 | 0.46 | 6.1 |
| 6 | CAM3 | cloud parameter $RH_{min}^{low} + 10\%$ | 232.2 | 0.44 | 6.3 |
| 6 | CAM3 | radius = $0.5 \times$ Earth's | 234.7 | 0.40 | 3.1 |
| 6 | CAM3 | radius = $1.0 \times$ Earth's | 230.0 | 0.44 | 3.7 |
| 6 | CAM3 | radius = $3.0 \times$ Earth's | 230.9 | 0.45 | 7.1 |
| 6 | CAM3 | gravity = 4.9 m s^{-2} | 235.9 | 0.44 | 7.3 |
| 6 | CAM3 | gravity = 9.8 m s^{-2} | 231.7 | 0.45 | 6.9 |
| 6 | CAM3 | gravity = 19.6 m s^{-2} | 230.6 | 0.44 | 6.5 |
| 6 | CAM3 | orbital period = 5 E-days | 248.2 | 0.34 | 14.4 |
| 6 | CAM3 | orbital period = 10 E-days | 246.1 | 0.36 | 12.0 |
| 6 | CAM3 | orbital period = 15 E-days | 234.6 | 0.42 | 8.2 |
| 6 | CAM3 | orbital period = 20 E-days | 230.5 | 0.45 | 8.0 |
| 6 | CAM3 | orbital period = 30 E-days | 230.6 | 0.45 | 7.6 |
| 6 | CAM3 | orbital period = 100 E-days | 229.6 | 0.46 | 6.1 |
| 6 | CAM3 | mixed layer depth = 1 m | 229.0 | 0.45 | 6.1 |
| 6 | CAM3 | mixed layer depth = 10 m | 229.8 | 0.46 | 6.3 |
| 6 | CAM3 | mixed layer depth = 100 m | 230.0 | 0.45 | 6.3 |
| 6 | CAM3 | surface pressure = 2 bars | 231.4 | 0.45 | 6.7 |
| 6 | CAM3 | surface pressure = 5 bars | 234.5 | 0.45 | 9.5 |
| 6 | CAM3 | surface pressure = 10 bars | 237.3 | 0.43 | 8.5 |
| 6 | CAM3 | $P_{(CO_2)} = 355 \text{ ppmv}$ | 237.5 | 0.45 | 11.0 |
| 6 | CAM3 | $P_{(CO_2)} = 0.01 \text{ bar}$ | 243.7 | 0.44 | 15.6 |
| 6 | CAM3 | $P_{(CO_2)} = 0.1 \text{ bar}$ | 252.3 | 0.44 | 21.8 |
| 6 | CAM3 | modern Earth continents I^j | 230.7 | 0.45 | 8.0 |
| 6 | CAM3 | modern Earth continents II^k | 228.5 | 0.46 | 6.6 |
| 6 | CAM3 | dayside-to-nightside OHT = 27 W m^{-2} | 235.4 | 0.44 | 7.9 |
| 6 | CAM3 | dayside-to-nightside OHT = 54 W m^{-2} | 239.5 | 0.41 | 7.5 |
| 6 | CAM3 | dayside-to-nightside OHT = 71 W m^{-2} | 249.5 | 0.38 | 11.5 |
| 6 | CAM3 | dayside-to-nightside OHT = 108 W m^{-2} | 258.8 | 0.36 | 17.0 |

^a T_S is the global-mean surface temperature.

^b Albedo is the planetary albedo, primary contributed from clouds.

^c G is the global-mean greenhouse effect.

^d Group 1, tidally locked cases, simulated by CAM3, CAM4 and CAM5. For these simulations, the sea-ice modules are switched off because there are significant differences in sea-ice simulation among these models. CAM3 has a resolution of $3.75^\circ \times 3.75^\circ$ and 26 vertical levels from the surface to $\approx 30 \text{ km}$. CAM4 and CAM5 have a horizontal resolution of $1.9^\circ \times 2.5^\circ$ and 26 and 30 vertical levels, respectively.

^e Group 2, tidally locked cases, simulated by CCSM3 without or with meridional barriers. The atmosphere component of CCSM3 is the same as CAM3. The ocean component has a variable latitudinal resolution starting at $\approx 0.9^\circ$ near the equator, a constant longitudinal resolution of 3.6° , and 25 vertical levels. The CCSM3 simulations have stronger greenhouse effect, this is due to that ocean heat transports from the dayside to the nightside and from the tropics to the extra-tropics of the dayside weaken or eliminate the temperature inversion.

^f Group 3, tidally locked cases with different stellar fluxes in CAM3. The default time step is 1800 s; for high stellar flux, it is reduced to 100 or 50 s to avoid numerical instability.

^g Group 4, non-tidally locked cases (2:1 spin-orbit resonance) in CAM3

^h Group 5, non-tidally locked cases (6:1 spin-orbit resonance) in CAM3

ⁱ Group 6, sensitivity tests for the tidally locked case in CAM3

^j The substellar point is set to 180°E over the Pacific Ocean.

^k The substellar point is set to 20°E over Africa.